M. Petrini, S. Seyedinnavadeh, V. Grimaldi, M. Milanizadeh, F. Zanetto, G. Ferrari, F. Morichetti, and A. Melloni, “Variable optical true-time delay line breaking bandwidth-delay constraints,” Opt. Lett., vol. 48, no. 2, p. 460-463, Jan. 2023, doi: 10.1364/OL.478102.

# Variable optical true-time delay line breaking bandwidth-delay constraints

Matteo Petrini,[1,*] Seyedmohammad Seyedinnavadeh,[1] Vittorio Grimaldi,[1] Maziyar Milanizadeh,[1,2] Francesco Zanetto,[1] Giorgio Ferrari,[1] Francesco Morichetti,[1] and Andrea Melloni[1]

[1]Department of Electronics, Information and Bioengineering, Politecnico di Milano, 20133 Milano, Italy
[2]Now with National Research Council, Ottawa, Canada
*Corresponding author: matteo.petrini@polimi.it

**Continuously variable true-time optical delay lines are typically subject to a constraint of the bandwidth-delay product, limiting their use in several applications. In this Letter, we propose an integrated topology that breaks the bandwidth-delay product limit. The device is based on multiple Mach–Zehnder Interferometers (MZIs) arranged in parallel, providing easier control and a larger bandwidth compared to ring resonator-based solutions. The functionality of this architecture is demonstrated with a 4-stage delay line by performing measurements in both the time and frequency domains. The delay line introduces a delay of 90 ps over a bandwidth of more than 22 GHz with a negligible group delay distortion, operates on a wavelength range of about 60 nm, and is scalable to a higher number of MZI stages.** 

https://doi.org/10.1364/-

Continuously variable optical true-time delay lines are a key element in a variety of applications from optical communications to optical computing and sensing, for both data synchronization [1] and data buffering [2]. Furthermore, in recent years delay lines have proved essential for novel microwave photonics systems [3] and optical beam-forming architectures for phased-array antennas [4], in particular to prevent beam squinting and to increase the bandwidth of the network [5]. Variable optical true-time delay lines can be implemented through different technologies, such as fiber-optics [6,7], free-space [8], and photonic integrated circuits (PICs).

In integrated optics, different circuit topologies have been proposed, grouped into two main categories: resonant and non-resonant structures. Resonant delay lines include photonic crystal waveguides (PCWs) and microring resonators (MRRs) [9]. PCW delay lines typically have a broad bandwidth but higher propagation loss (dB/cm or dB/ps), thus being more suitable for delaying short pulses [10]. MRR-based delay lines can achieve group delays of up to hundreds of picoseconds in a reduced footprint, but with narrower bandwidth and large chromatic dispersion [11]. Coupled-resonator structures [10] can enlarge the bandwidth at the expense of a large number of cavities, but their control algorithm is quite complex. Moreover, MRR-based structures can be affected by detrimental nonlinear effects due to intra-cavity field enhancement. Non-resonant delay lines offer a good trade-off between large operational bandwidth, simple control, high resilience to nonlinearities, lower group delay dispersion, and requiring a larger footprint [12]. Grating-based delay lines offer a small footprint and wide delay tunability, but bandwidth constraints and/or limited flexibility in delay reconfiguration [9,13]. Discrete tuneability of the group delay is typically achieved with switchable delay lines [14]. Mach–Zehnder Interferometer (MZI)-based delay lines with tunable couplers (TCs) can be used to introduce a continuously tunable delay [15,16]. However, both MRR-based and MZI-based delay lines are subject to a constraint of the bandwidth-delay product [9,12], because a longer delay is achieved at the expense of narrower operating bandwidth [15,17]. For example, a single unbalanced MZI shows a minimum bandwidth-delay product of 0.25 [15], while a ring resonator is about three times lower [11]. In this Letter we propose a novel architecture, based on parallel MZIs, capable of introducing a continuously variable true-time delay, breaking the bandwidth-delay product limit (achieving up to 1.75 in the worst bandwidth-wise case). The presented device is realized in silicon photonics and is equipped with a suitable electronic control board, including both custom electronics and software.

The topology of the proposed delay line is sketched in Fig. 1(a). It is composed of four parallel unbalanced MZIs, configured in such a way that the longer arm of the Nth stage is the reference arm of the (N + 1)th MZI. Every single stage is implemented by means of two balanced MZI-based TCs, whose power coupling ratio, $K_A$ and $K_B$, can be continuously varied from 0 to 1. The combined use of heaters and photodetectors, the latter labeled as $PD_{Ai}$ and $PD_{Bi}$, and placed at one of the TC outputs (or through a 10% tap), permits an effective and fine control of the coupling ratio. In Fig. 1(a) the index $i = 1, 2, 3, 4$ refers to the stage. Each MZI stage has an unbalance $\Delta L$ between the two arms, and a thermo-optic phase shifter $H_i$ ($i = 1, 2, 3, 4$) allows a precise frequency tuning, to match the central wavelength of the input signal. The number of MZI stages can be increased to achieve longer delays. At the central operative frequency, when the MZI is in bar condition, each single stage

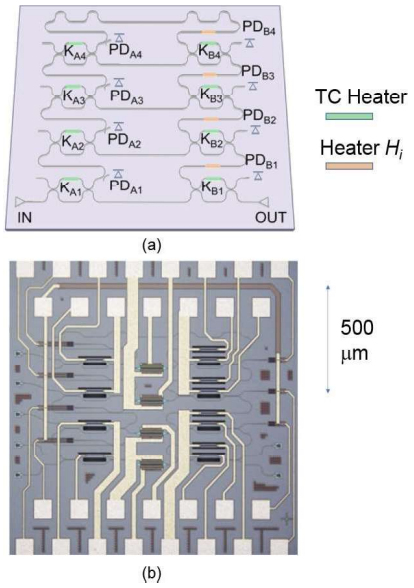


**Fig. 1.** (a) Schematic of the proposed tunable delay line based on parallel MZIs; (b) photograph of the realized device on a silicon photonics platform.

can provide a maximum time delay given by

$$T_{MZ} = \frac{n_g \Delta L}{c} = \mathrm{FSR}^{-1}, \quad (1)$$

where $\Delta L$ is the geometrical unbalance of each MZI, $n_g$ the waveguide group index, $c$ is the vacuum speed of light, and FSR is the Free Spectral Range. In MZI-based delay lines, the time delay is a linear function of the coupling coefficient of the TCs [15] and the actual introduced delay is $T_D = \mathrm{K} T_{MZ}$ where $\mathrm{K} = \mathrm{K_A} = \mathrm{K_B}$. To induce a generic delay $T_D$ between 0 and $T_{MZ}$, the couplers $\mathrm{K_{A2}}$ and $\mathrm{K_{B2}}$ have to be set to 0 (i.e., both in bar condition), while $\mathrm{K_{A1}}$ and $\mathrm{K_{B1}}$ are set to the value $T_D/T_{MZ}$. In this case, only the first stage of the device is operative as a delay line, while the upper stages are completely isolated. In the case of $T_D$ between $T_{MZ}$ and $2T_{MZ}$, the couplers $\mathrm{K_{A1}}$ and $\mathrm{K_{B1}}$ have to be set to 1 (i.e., both to cross condition), while $\mathrm{K_{A3}} = \mathrm{K_{B3}} = 0$ isolates the third stage and $\mathrm{K_{A2}}$ and $\mathrm{K_{B2}}$ are set to the desired working point. In this case, the second stage behaves as an MZI-based delay line while the first stage contributes with the maximum delay $T_{MZ}$ given by Eq. (1). Generalizing this procedure for an arbitrary number of stages, it is convenient to introduce the integer part $M$ and mantissa $m$ of the ratio $T_D/T_{MZ}$,

$$M = 1 + \frac{T_D}{T_{MZ}}, m = \frac{T_D - (M-1)T_{MZ}}{T_{MZ}} = mant\left(\frac{T_D}{T_{MZ}}\right). \quad (2)$$

The tunable couplers $\mathrm{K_{A}}_i = \mathrm{K_{B}}_i$, $i$ being an integer between 1 and $M$–1, are set to 1 to be in cross condition and introduce a delay equal to $(M-1)T_{MZ}$. Conversely, $\mathrm{K_{A(M+1)}} = \mathrm{K_{B(M+1)}} = 0$ sets the bar condition to isolate the last stages and $\mathrm{K_{AM}} = \mathrm{K_{BM}} = m$ fine adjust the delay to $T_D$. In this way, the $M$th MZI is the only stage that actually works as an interferometer and sets the residual delay $mT_{MZ}$. The maximum delay is achieved when all the TCs are in cross condition so that the optical signal propagates through the longest path. The key aspect is that, irrespective of the total delay, only one MZI operates as an interferometer, enabling the constraint to be broken on the bandwidth-delay product. In any condition the 3 dB bandwidth ($B_{3dB}$) of the delay line is therefore equal to or larger than FSR/2, as for a single stage MZI-based delay line [15].

A top view microphotograph of the device fabricated by Advanced Micro Foundry (AMF) [18] in a commercial silicon platform is shown in Fig. 1(b). Its footprint is 1.2 mm by 0.6 mm (1.2 mm by 1.25 mm including electrical pads). The silicon channel waveguides have a dimension of 500 nm by 220 nm on a 3-µm-thick silica BOX substrate. The standard Process Design Kits (PDKs) for the I/O grating couplers and PDs have been adopted. TiN heaters are placed 700 nm above the waveguide to maximize the thermo-optic efficiency with no impact on the optical loss. In the presented device, $\Delta L = 1.73$ mm, $n_g = 3.90$ at 1550 nm, $T_{MZ} = 22.5$ ps, and FSR = 44.4 GHz. The bandwidth of the single MZI stage is $B_{3dB} = 22.2$ GHz. The four MZI stages provide a maximum delay $T_{Dmax} = 4T_{MZ} = 90$ ps.

The TCs are implemented by means of a balanced MZI with two 50:50 directional couplers and an 85-µm-long thermo-optic phase shifter integrated into one arm of the MZI to achieve the full tuneability of the equivalent coupling ratio K. The MZI-based TC is robust against fabrication tolerances and wavelength dispersion of the direction couplers, and can be tuned to provide the desired power split ratio at a target wavelength across a wavelength range of tens of nanometers [19]. Figure 2(a) shows the dependence of K and 1–K of a TC as a function of the electrical power dissipated by its heater with a resistance of 340 Ω. When no current is fed to the actuator, the TC is almost in cross condition, as expected by the design. Figure 2(b) shows the wavelength dependence of K between 1520 nm and 1580 nm when the TC is tuned to the cross condition at 1520 nm (measurement is normalized with respect to a reference straight waveguide terminated with the same I/O grating couplers); the spectral behavior is almost constant over 60 nm (see Supplement 1 Fig. S1), this setting being the operational wavelength range of the whole PIC. The integrated Ge photodetectors $\mathrm{PD_{A}}_i$ and $\mathrm{PD_{B}}_i$ are used to calibrate and control the delay line [18].

In order to effectively tune the PIC, a custom electronic controller was developed. The monitor signals are acquired by the PDs shown in Fig. 1(a) and are connected to an acquisition chain composed by logarithmic transimpedance amplifiers, an antialiasing filter, and analog to digital converters, calibrated to ensure a correct power estimation. The control of the delay line is automatically achieved with the following procedure. Let's consider the two parameters $M$ and $m$ of Eq. (2) that define the desired delay. First, the $M$–1 TC pairs are tuned in cross condition by maximizing the power detected by $\mathrm{PD_{A}}_i$ and minimizing $\mathrm{PD_{B}}_i$ (with $i$ between 1 and $M$–1).

At the same time, $\mathrm{K_{A(M+1)}}$ and $\mathrm{K_{B(M+1)}}$ are set to 0 by minimizing the power detected by $\mathrm{PD_{A(M+1)}}$ and $\mathrm{PD_{B(M+1)}}$. At this point, the condition $\mathrm{K_{AM}} = \mathrm{K_{BM}} = m$ has to be achieved.

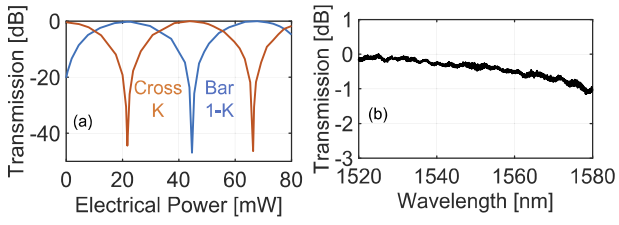


**Fig. 2.** (a) Equivalent coupling coefficient of a TC versus heater electrical power for the two ports: bar (K) and cross (1–K). (b) Normalized wavelength dependence of the TC when the coupling coefficient is set to K = 1 (cross port), at 1520 nm.

To this end, the power detected by $PD_{AM}$ is maximized (i.e., $K_{AM} = 1$), and the heater of $K_{BM}$ is finely calibrated in such a way that the ratio between the detected power $PD_{BM}/PD_{AM}$ is equal to $1-m$ (at the steady state and net of extra insertion losses). Then, the actuator that sets the coupling ratio $K_{AM}$ is controlled to make the power ratio $PD_{AM}/PD_{A(M-1)}$ equal to $m$. At the same time, if necessary, the central operative wavelength is recovered with the phase shifter $H_M$ by maximizing the power at the Out port. The accuracy of the induced time delay depends mainly on the precision of the optical power reading, and hence on the PDs and signal acquisition chain quality, and typically is well below 1 ps. By relying on optical power ratios rather than on absolute power measurements, the control and calibration procedure is robust against possible fluctuations of the input signal power (except for the case $M = 1$, but this issue is solved by placing a 1% tap-PD at the input port). The entire iterative procedure lasts only a few tens of milliseconds thanks to the application of the Thermal Eigenmode Decomposition (TED) technique, described in Ref. [20], that mitigates the thermal coupling among heaters. The most pronounced thermal coupling (about 5%) is observed between the pairs $H_j$ and $K_{Bj}$, that are spaced by about 45 µm. The procedure can be applied for testing and look-up table generation, and also for control and locking during operation.

The spectral response of the tunable delay line has been characterized by means of a Tunable Laser Source (TLS, ANDO 4320) synchronized with an Optical Spectrum Analyzer (OSA, ANDO 6317). The experiment has been performed for $M = 1$, 2, 3, 4 and for $m = 0$, 0.25, 0.5, 0.75 and also for the longest path, corresponding to $M = 4$ and $m = 1$. The measured In-Out magnitude transmission spectra are shown in Fig. 3(a). Each single plot per color is related to a different value of $M$. Regardless of the order $M$ of tuned stages, the In-Out transfer function of the circuit always behaves as a single MZI with an FSR of 356 pm (or 44.4 GHz at 1550 nm). The narrowest 3dB-bandwidth occurs, as for a single stage delay line for $K_{Ai} = K_{Bi} = 0.5$ [15], and it is equal to FSR/2 = 178 pm (22.2 GHz). Figure 3(b) shows

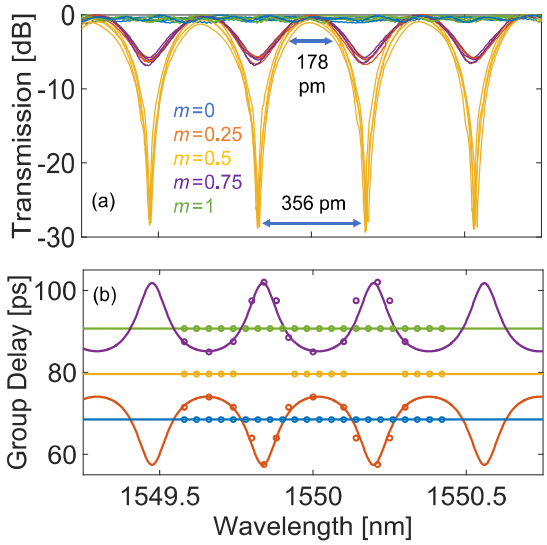


**Fig. 3.** (a) Normalized transmission spectra of the proposed delay line for different values of $m$ (0, 0.25, 0.5, 0.75, 1), and for different values of $M$ (1, 2, 3, 4). Each individual line per color represents a different value for capital M. (b) Group delay spectra for $M = 4$ and for the same values of $m$ [colors are matched with those of Fig. 3(a)]. Solid lines show analytical results; markers indicate experimental results.

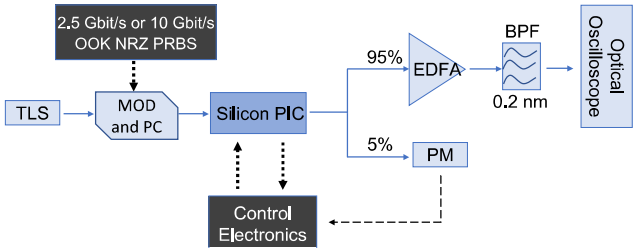


**Fig. 4.** Block scheme of the experimental setup used for time domain measurements. The modulated signal is coupled to the silicon photonic chip through a polarization controller (PC). The output signal is amplified by an erbium doped fiber amplifier (EDFA), filtered with a bandpass filter (BPF, 0.2 nm bandwidth), and acquired with an optical oscilloscope.

the experimentally estimated spectral group delay characteristic compared with the theoretical behavior [15] for $M = 4$ and $m = 0$, 0.25, 0.5, 0.75, 1 [colors are matched with those in Fig. 3(a)]. The setup used for the measurement of the group delay is shown in Fig. 4. The optical carrier wavelength provided by the TLS is modulated by a 2.5 Gbit/s OOK NRZ PRBS signal (On-Off Keying, Non-Return to Zero, Pseudo-Random Binary Sequence). The modulated optical signal has a bandwidth more than ten times narrower than the minimum 3dB-bandwidth of the circuit. The true-time delay, with respect to the reference path, has been directly measured with an optical oscilloscope (Tektronix CSA8200). The measurement was repeated by shifting the carrier wavelength of the optical signal over more than one FSR, with wavelength steps of around 40 pm (5 GHz). The measured group delay is averaged over the probe signal bandwidth and matches the expected behavior [Fig. 3(b)]. The experiment has been conducted for five different cases, corresponding to the five different values of $k$ accounted before ($m = 0$, 0.25, 0.5, 0.75, 1). The same behavior is valid for lower values of $M$ but shifted by integer multiples of $T_{MZ}$. At the central operative wavelength (1550.03 nm), the maximum achievable delay is 90 ps. The dependence of the group delay with respect to the different pairs of TCs is shown in Fig. 5 (blue markers, fitted by the dashed-dotted line). As the four different stages are activated (i.e., sequential tuning of the TCs) the delay linearly increases from 0 ps to 90 ps. The total insertion loss of the circuit increases in proportion, as shown by the orange markers. The maximum signal power reduction, with respect to the reference path, is around 3 dB, which is due to the waveguide propagation loss (1.3 dB/cm), the four 10%-taps (0.45 dB each), and TCs (0.05 dB each). The scaling of the architecture to a large number of stages is limited by the insertion loss that can be substantially reduced by using tap-PD with a lower coupling ratio at the expense of a reduced accuracy in the tuning of the delay. Another suitable solution could be the use of transparent detectors [21].

The impact of the variable delay line on data transmission in terms of insertion loss and signal distortion was tested on a 10 Gbit/s OOK NRZ modulated signal using the setup of Fig. 4. The signal carrier is tuned at a wavelength of 1550.03 nm and the delay line is controlled in order to have the minimum the insertion loss and the minimum group delay distortion around this wavelength. By continuously controlling the TCs, the signal can be arbitrarily delayed up to 1 bit time with neither degradation in transmission quality nor distortion of the eye-shape, as shown in Figs. 6(a)–6(c). Only signal amplitude is affected by total device attenuation—as shown in the pictures, power reduction is recovered by the optical amplifier working in

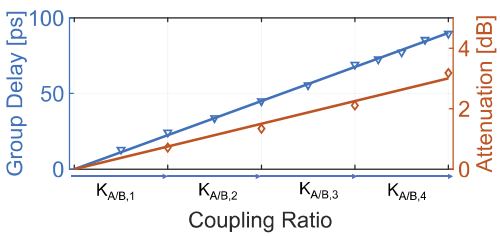


**Fig. 5.** Simulated (dashed-dotted lines) and measured (markers) group delay (triangles) and attenuation (diamonds) introduced by the delay line when the TC pairs span from 0 to 1.

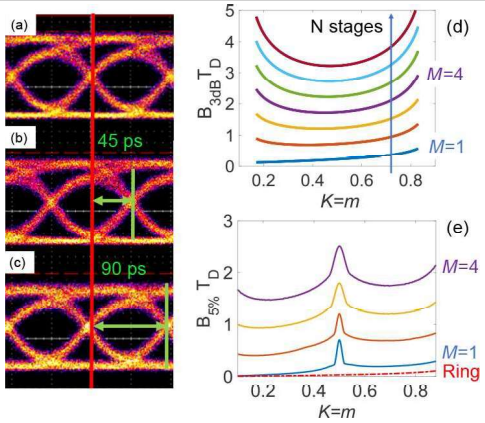


**Fig. 6.** Eye diagram of a 10 Gbit/s signal when (a) it propagates through the shortest path of the delay line, (b) it is tuned for the condition $M = 3$, $m = 0$ (45 ps delay, equal to half of the maximum delay), and (c) it propagates through the longest path (90 ps delay). (d) Bandwidth-delay product as a function of $m$ (where the 3-dB band can be defined, i.e., for $m > 0.83$ or $m < 0.17$), for different number of stages N. Proposed architecture (violet, $M = 4$) is well above the single MZI (blue, $M = 1$). Dashed-dotted lines show the expected behavior for increasing N. (e) Same as (d) but defining the bandwidth where the group delay varies less than 5% (with respect to the central wavelength value) [15].

saturation mode. This result proves that the proposed delay line allows us to overcome the bandwidth-delay product $BT_D$ because the delay can be increased linearly with the number of the MZI stages without narrowing the bandwidth. Such a characteristic cannot be achieved with a single MZI or ring resonator [15,17]. The bandwidth-delay product $B_{3dB}T_D$ of a delay line with $M$ stages against the coupling coefficient $K = K_A = K_B = m$ is given in Fig. 6(d). Defining the bandwidth as the wavelength interval where the group delay changes less than 5% with respect to the central wavelength value [15], the bandwidth-group delay product ($B_{5\%}T_D$) dependence against coupling ratio, for a different number of stages, is reported in Fig. 6(e). The benefit of MZI-based delay lines with respect to all pass ring resonators (red line) becomes more and more evident as the number of stages increases. The data of those plots can be found in Dataset 1, Ref. [22].

In conclusion, we present a novel architecture for an integrated delay line enabling the introduction of a continuously variable true-time optical delay. The proposed topology is based on parallel MZIs and that breaks the inherent bandwidth-delay product of conventional structures. With four MZIs, a tunable delay range of 90 ps is demonstrated with a $B_{3dB}$ larger than 22 GHz. Higher delays can be achieved by using more MZIs with no bandwidth narrowing. The structure can be calibrated by exploiting a simple and fast control strategy providing a delay accuracy of 0.1ps, which is mostly limited by the accuracy of the PD acquisition, over a broad wavelength range of about 60 nm, which is more than the extended telecom C-band. Relying on non-resonant elements, it is inherently more resilient to non-linear phenomena with respect to cavity-assisted architectures made in the same photonic platform [23].

**Funding.** Agenzia Nazionale per l'attrazione degli investimenti e lo sviluppo d'impresa S.p.A., EnTER project, Invitalia (0139934).

**Acknowledgments.** The Authors acknowledge the staff of Polifab, the microelectronic facility of Politecnico di Milano, for the support in the assembly of photonic chips.

**Disclosures.** The Authors declare no conflict of interest.

**Data availability.** Data underlying the results presented in this paper are available in Dataset 1, Ref. [22].

**Supplemental document.** See Supplement 1 for supporting content.

## REFERENCES

1. A. Melloni, F. Morichetti, C. Ferrari, and M. Martinelli, Opt. Lett. **33**, 2389 (2008).
2. F. Xia, L. Sekaric, and Y. Vlasov, Nat. Photonics **1**, 65 (2007).
3. J. F. Diehl, J. M. Singley, C. E. Sunderman, and V. J. Urick, Appl. Opt. **54**, F35 (2015).
4. C. Tsokos, E. Andrianopoulos, A. Raptakis, N. K. Lyras, L. Gounaridis, P. Groumas, R. B. Timens, I. Visscher, R. Grootjans, L. S. Wefers, D. Geskus, E. Klein, H. Avramopoulos, R. Heideman, C. Kouloumentas, and C. G. H. Roeloffzen, J. Lightwave Technol. **39**, 5845 (2021).
5. R. Rotman, M. Tur, and L. Yaron, Proc. IEEE **104**, 504 (2016).
6. C. Caucheteur, A. Mussot, S. Bette, A. Kudlinski, M. Douay, E. Louvergneaux, P. Mégret, M. Taki, and M. González-Herráez, Opt. Express **18**, 3093 (2010).
7. M. González Herráez, K. Yong Song, and L. Thévenaz, Opt. Express **14**, 1395 (2006).
8. M. Yessenov, B. Bhaduri, P. J. Delfyett, and A. F. Abouddary, Nat. Commun. **11**, 5782 (2020).
9. B. Paul, K. Sertel, and N. K. Nahar, IEEE Access **10**, 75513 (2022).
10. A. Melloni, A. Canciamilla, C. Ferrari, F. Morichetti, L. O'Faolain, T. F. Krauss, R. De La Rue, A. Samarelli, and M. Sorel, IEEE Photonics J. **2**, 181 (2010).
11. J. Cardenas, M. A. Foster, N. Sherwood-Droz, C. B. Poitras, H. L. R. Lira, B. Zhang, A. L. Gaeta, J. B. Khurgin, P. Morton, and M. Lipson, Opt. Express **18**, 26525 (2010).
12. D. Lin, S. Shi, W. Cheng, P. Liu, M. Lu, T. Lin, G. Hu, B. Yun, and Y. Cui, Journal of Lightwave Technology **41**, 209(2022).
13. J. Wang, R. Ashrafi, R. Adams, I. Glesk, I. Gasulla, J. Capmany and, and L. R. Chen, Sci. Rep. **6**, 30235 (2016).
14. P. Zheng, X. Xu, D. Lin, P. Liu, G. Hu, B. Yun, and Y. Cui, Optics Communications, **488**126842 (2021).
15. D. Melati, A. Waqas, Z. Mushtaq, and A. Melloni, IEEE J. Sel. Top. Quantum Electron. **24**, 4400108 (2018).
16. Z. Mushtaq, M. A. Uqaili, A. Waqas, and B. S. Chowdhry, Wireless Pers. Commun. **121**, 1221 (2021).
17. A. Waqas, D. Melati, and A. Melloni, IEEE Photonics Technol. Lett. **30**, 1830 (2018).
18. "PDK of AMF," Advanced Micro Foundry, 2022, http://www.advmf.com.
19. D. A. B. Miller, Optica **2**, 747 (2015).
20. M. Milanizadeh, D. Aguiar, A. Melloni, and F. Morichetti, J. Lightwave Technol. **37**, 1325 (2019).
21. S. Grillanda, M. Carminati, F. Morichetti, P. Ciccarella, A. Annoni, G. Ferrari, M. Strain, M. Sorel, M. Sampietro, and A. Melloni, Optica **1**, 129 (2014).
22. M. Petrini, S. Seyedinnavadeh, V. Grimaldi, M. Milanizadeh, F. Zanetto, G. Ferrari, F. Morichetti, and A. Melloni, "Variable optical true time delay line breaking bandwidth-delay constraints - dataset," Zenodo: Version 1, 11 October 2022, https://doi.org/10.5281/zenodo.7219891.
23. M. Petrini, M. Milanizadeh, F. Morichetti, and A. Melloni, Opt. Lett. **46**, 5023 (2021).